Nanoscale

Computational Approach for Structure Generation of Anisotropic Particles (CASGAP) with Targeted Distributions of Particle Design and Orientational Order

Journal:	*Nanoscale*
Manuscript ID	NR-ART-05-2023-002425.R1
Article Type:	Paper
Date Submitted by the Author:	05-Aug-2023
Complete List of Authors:	Gupta, Nitant; University of Delaware, Chemical and Biomolecular Engineering Jayaraman, Arthi; University of Delaware, Chemical and Biomolecular Engineering

ARTICLE

Computational Approach for Structure Generation of Anisotropic Particles (CASGAP) with Targeted Distributions of Particle Design and Orientational Order

Received 00th January 20xx,
Accepted 00th January 20xx

DOI: 10.1039/x0xx00000x

Nitant Gupta[a] and Arthi Jayaraman*[a,c]

The macroscopic properties of materials are governed by their microscopic structure which depends on the materials' composition (i.e., building blocks) and processing conditions. In many classes of synthetic, bioinspired, or natural soft and/or nano materials, one can find structural anisotropy in the microscopic structure due to anisotropic building blocks and/or anisotropic domains formed through the processing conditions. Experimental characterization and complementary physics-based or data-driven modeling of materials' structural anisotropy is critical for understanding structure-property relationships and enabling targeted design of materials with desired macroscopic property. In this pursuit, to interpret experimentally obtained characterization results (e.g., scattering profiles) of soft materials with structural anisotropy using data-driven computational approaches, there is a need for creating real space three-dimensional structures of the designer soft materials with realistic physical features (e.g., dispersity in building blocks' sizes) and anisotropy (i.e., aspect ratios of the building blocks, their orientational and positional order). These real space structures can then be used to compute and complement experimentally obtained characterization results or be used as initial configurations for physics-based simulations/calculations that can then provide training data for machine learning models. To address this need, we present a new computational approach called CASGAP - Computational Approach for Structure Generation of Anisotropic Particles - for generating any desired three dimensional real-space structure of anisotropic building blocks (modeled as particles) adhering to target distributions of particle shape, size, and positional and orientational order.

Introduction

Materials comprising of polymers, colloids, and suspended nanoparticles, termed collectively as 'soft materials' exhibit structural diversity at a range of length scales starting from their molecular dimensions (~1 Å - 10 nm) to assembled domains of sizes ~100 nm – 10 μm. This structural diversity in soft materials is driven by the nature and strength of the intermolecular interactions (e.g., van der Waals, electrostatic, hydrogen bonding, etc.) between the various chemical species and can also be affected by their processing conditions (e.g., thermal, solvent(s), mechanical stresses, or chemical stimuli). In particular, the interplay of interactions and processing can strongly affect the positional and orientational order within these mostly amorphous soft material structures that exhibit features somewhere between crystalline solids and completely disordered liquids[1]. In crystalline solids, the structure is highly resilient to room temperature fluctuations due to their stronger, long-ranged interactions as compared to disordered liquids whose structure can fluctuate both in space and time with little to no ordering at short ranges. As intermediates, amorphous soft materials can exhibit distribution in the shapes and sizes of their internal structure as well as in the extent of their positional and orientational order. Subtle changes to these morphological features can have a significant impact on the physical properties of soft materials; thus, to create structure-property relationships in soft materials the distribution of structural features must be modelled and characterized with great nuance and precision.

In modeling studies of soft materials, the structural elements – the molecular building blocks or the assembled domains of molecules – are often treated as hard or soft particles, either via coarse-grained models or via multi-phase models[2–4]. These particles' chemistry, shapes, and sizes, as well as their positional correlations (i.e., order/disorder), can be linked to the physical properties of the structure (namely, mechanical[5–8], optical/photonic[9–12], electronic/magnetic[13,14] and transport within[15,16]) through additional physics-based modeling and simulation methods or for further experiments. Importantly, when the structural elements are anisotropic in shape (e.g., rod-shaped nanoparticles, crystalline domains in polymers, liquid crystalline domains) then the extent of orientational order in addition to positional order can become an important consideration for calculating physical properties. To establish the materials design – structure – property relationships, one

[a] Department of Chemical and Biomolecular Engineering, 150 Academy St, University of Delaware, Newark, DE 19716 USA.
[b] Department of Materials Science and Engineering, 201 Dupont Hall, University of Delaware, Newark, DE 19716 USA.
*Corresponding author arthij@udel.edu
Electronic Supplementary Information (ESI) available: [details of any supplementary information available should be included here]. See DOI: 10.1039/x0xx00000x

must quantify and characterize the extent of positional and orientational structural order within the material for various sets of particle designs (e.g., chemistry, size, shape) and processing techniques.

Characterization of Positional and Orientational Order in Soft Materials

In **Figure 1** we show examples of diverse soft materials' structures observed in experiments with different degrees of positional and orientational order that vary independently or in a coupled manner. These examples show (a) both positional and orientational ordering to control the thickness[17] of the assembled structure, or to demonstrate monodispersity[18]; (b) only orientational ordering to achieve a property (curvature) for controllable phase behavior[19], or to study preferential alignment during fluid flow[20]; and (c) weak positional ordering to pack anisotropic building blocks into superstructures[21], or to understand mechanical (shear) behavior of colloidal monolayers[22]. Many classes of soft materials, however, (d) lack both positional and orientational ordering, leading to amorphous structures as in the case of nanoparticle dispersions[23] or polymeric networks[24]. Furthermore, in biological/naturally occurring soft materials there could also be cross correlation between positional and orientational ordering that gives rise to specific functionality or property of that material. This idea has been depicted schematically in (e) with the circular organization of the anisotropic elements in the form of cells or their organelles[25,26]. Such correlated (or lack of correlated) positional and orientational organization can have biological implications, like the example in ref.[26] where hexagonal cell shape improves cell cohesion whereas round or oval cells form loose aggregates.

To characterize positional and orientational order in soft materials, researchers use direct imaging techniques, like scanning or transmission electron microscopy (SEM/TEM). However, these techniques are not appropriate for studying structural dynamics and/or structural features at multiple length scales simultaneously, and can be destructive due to requisite pre-treatment like drying, freezing or sectioning[27,28]. Indirect characterization techniques like scattering (by light, X-rays, or neutrons) can overcome the aforementioned challenges with direct imaging. However, these indirect techniques often provide structural information in the reciprocal (Fourier) space. Interpretation of the results from such indirect structural characterization methods is not trivial, especially when the structure is amorphous and exhibits some positional and orientational order. In the case of crystalline structure, the periodicity can aid the interpretation of the structure by identification of known characteristic peaks. In the case of non-crystalline structures (**Figures 1b-e**), the interpretation of scattering profiles is not always straightforward and involves either tedious fitting to relevant analytical models[29] of scattering profiles or in case of absence of analytical models, optimization of a modeled structure

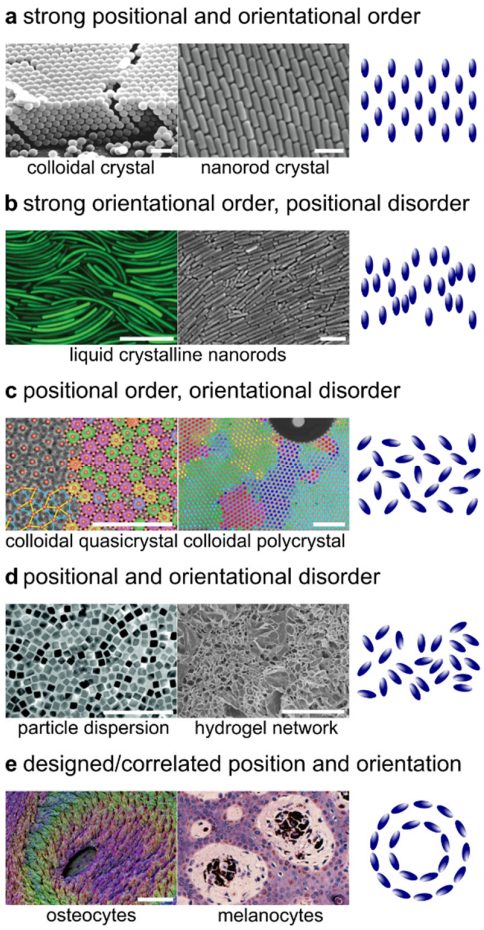

Figure 1 Examples of synthetic or biologically relevant soft materials exhibiting different extents of positional and orientational order/disorder. (a) Colloidal (left) and nanorod (center) crystals exhibiting strong positional and orientational order. Left image adapted with permission from [17]. Copyright 1999 American Chemical Society. Center image adapted with permission from [18]. Copyright 2012 American Chemical Society. (b) Liquid crystalline-type assemblies of banana-shaped nanorods (left) and straight nanorods (center) exhibiting local or large scale orientational order. Left image adapted from [19]. Reprinted with permission from AAAS. Center image adapted with permission from [20]. Copyright 2006 American Chemical Society. (c) Colloidal assemblies as quasicrystal (left) or polycrystal (center) with some positional order. Left image adapted from [21]. Reprinted with permission from AAAS. Center image adapted with permission from [22]. Copyright (2017) by the American Physical Society. (d) Amorphous structures like nanoparticle dispersion (left) and polymer network (center) with no positional or orientational order. Left image adapted with permission from [23]. Copyright 2007 American Chemical Society. Center image adapted from [24]. Reproduced with permission from Springer Nature. (e) Biological tissues with nanoscale organelles, i.e., osteocytes (left) and melanocytes (center) that occur in a designed/tailored arrangement. Left image adapted from [25]. Reproduced with permission from Springer Nature. Center image adapted from [26]. Reproduced with permission from Springer Nature. The scale bars values (in μm) are (a) 1, 0.1; (b) 10, 0.1;(c) 0.1, 50; (d) 0.1, 50; and (e) 10.

generated through computational methods like reverse Monte Carlo[30,31] or Computational Reverse Engineering Analysis of Scattering Experiments (CREASE)[32]. These computational methods interpret the scattering results by identifying structure (or structures) whose computed scattering profile matches the experimentally obtained scattering profiles. The success of such computational methods relies on being able to generate a range of three dimensional (3D) real space structures with

incremental variations to structural features (e.g., particle positions, sizes, shapes, and orientations). These 3D structures can be (i) used directly for optimizing towards a structure that exhibits the best match between the computed and experimental scattering profiles or (ii) used along with their computed scattering profiles together as training data for machine learning models that link descriptions of these 3D structures to their computed scattering profile.[33–35] In particular for the latter case of data-driven approaches, computationally efficient generation of 3D real space structures requires a lower dimensional representation of the structure that can capture the desired distributions in the structural features without manually doing such variation for each and every individual particle.

In the case of spherical particles, many algorithms can be found in literature[36–39] for modeling the particles' desired size dispersity and these algorithms can be coupled with stochastic or deterministic molecular simulations (e.g., Monte Carlo, molecular dynamics, Brownian dynamics etc.) to achieve a desired 3D structure for these spherical particles. However, classical stochastic or deterministic simulation methods tend to access equilibrium configurations, or a limited number of kinetically trapped configurations (due to poor sampling) and require knowledge of inter-particle interactions within the complex material that one may not know *a priori*. Moreover, it is difficult to capture anisotropic structural details of the assembled spherical particles unless the particles can be clustered together meaningfully, which can pose additional computational challenges.

In the case of non-spherical particles, far fewer number of papers[40–43] have addressed construction of 3D structures with anisotropic structural elements at desired packing fractions. We highlight here two such noteworthy studies for 3D structural creation for non-spherical particles – In one study, Torquato and co-workers[40] developed the "adaptive shrinking cell method", which enables them to construct dense packing of arbitrary shaped particles. However, their method currently may not preserve desired particle orientational order as the particles are allowed to freely rotate to achieve higher packing efficiency. Thus, it is not suitable for creating structures with a specific positional or orientational order that may only be accessed through processing techniques. Another method by Jia et al.[41] describing packing of arbitrary shapes, can preserve particle orientation, however it is based on a grid, requiring digitization of the entire simulation cell, which can be computationally intensive for large system sizes. To the best of our knowledge, there are no other studies that describe computational methods to build 3D structures of anisotropic particles with target distributions of particle shapes and sizes exhibiting desired positional and orientational order.

In this paper we present a new computational workflow - **Computational Approach for Structure Generation of Anisotropic Particles (CASGAP)** - that can generate 3D structures of anisotropic particles with target distributions of particle shapes and sizes exhibiting desired positional and orientational order. We describe the anisotropic particles' sizes, shapes and orientations via well-defined statistical models or probability distributions. In particular, we formalize the distribution of orientational order by using the von Mises-Fisher distribution which has rarely been used in the context of soft materials[44,45]. We demonstrate that for some of these parameters, in place of a distribution, a more complex spatial field-based description can also be imposed to add spatial correlations, aiding in modeling of sophisticated or hierarchical structures. We tackle unique challenges that one faces with non-spherical particles that are not an issue when dealing with spherical particles, including determining overlap between two particles which can be highly specific to the shape of the individual particles. In a way, this new CASGAP method can be viewed as an adaptation of the random sequential adsorption (RSA) type algorithms[41,46] but for anisotropic particles with polydispersity in shapes, sizes and orientations. Further, CASGAP is inspired from algorithms with sophisticated computational advances for aerospace engineering and video-game design that deal with collision-detection of arbitrary geometries at scale and with computational efficiency. We make use of these algorithms from these other fields to efficiently detect and resolve inter-particle overlaps in our soft materials structure generation work. CASGAP also facilitates the user to invest only the computational resources that they have available by stopping the algorithm as and when needed and yet achieving structures adhering to the targeted statistical distributions of particle size, shape, and order.

CASGAP will be valuable for experimentalists and computational researchers using data-driven and physics-based models. As described earlier, in computational methods used for interpretation of scattering results (e.g., CREASE), there is a need for real space structure generation to identify features of structures that give rise to the scattering patterns; CASGAP can be used for this purpose. With the advent of data driven and machine learning methods, CASGAP can be used for generating large databases of 3D structures with various minor or major variations in particle shapes, sizes, and positional and orientational order parameters; this type of database is essential for the training of machine learning models for design-structure or structure-property relationships. CASGAP can also be useful for creating desired (experimentally relevant) initial configurations for use in molecular dynamics simulations, in particular for predicting dynamic evolution upon application of a stimulus on one experimentally observed 'processed' structure to another structure. Although, it is possible to use molecular simulations to also create 3D structure with anisotropic potentials for anisotropic particles, the resultant structures may not preserve desired orientation of particles that one may achieve only through processing and not via thermodynamics. Our approach generates 3D non-crystalline configurations regardless of whether it is an equilibrium configuration accessible to simulations or non-equilibrium configuration accessed through unique processing pathways in experiments. We acknowledge that some notable and widely

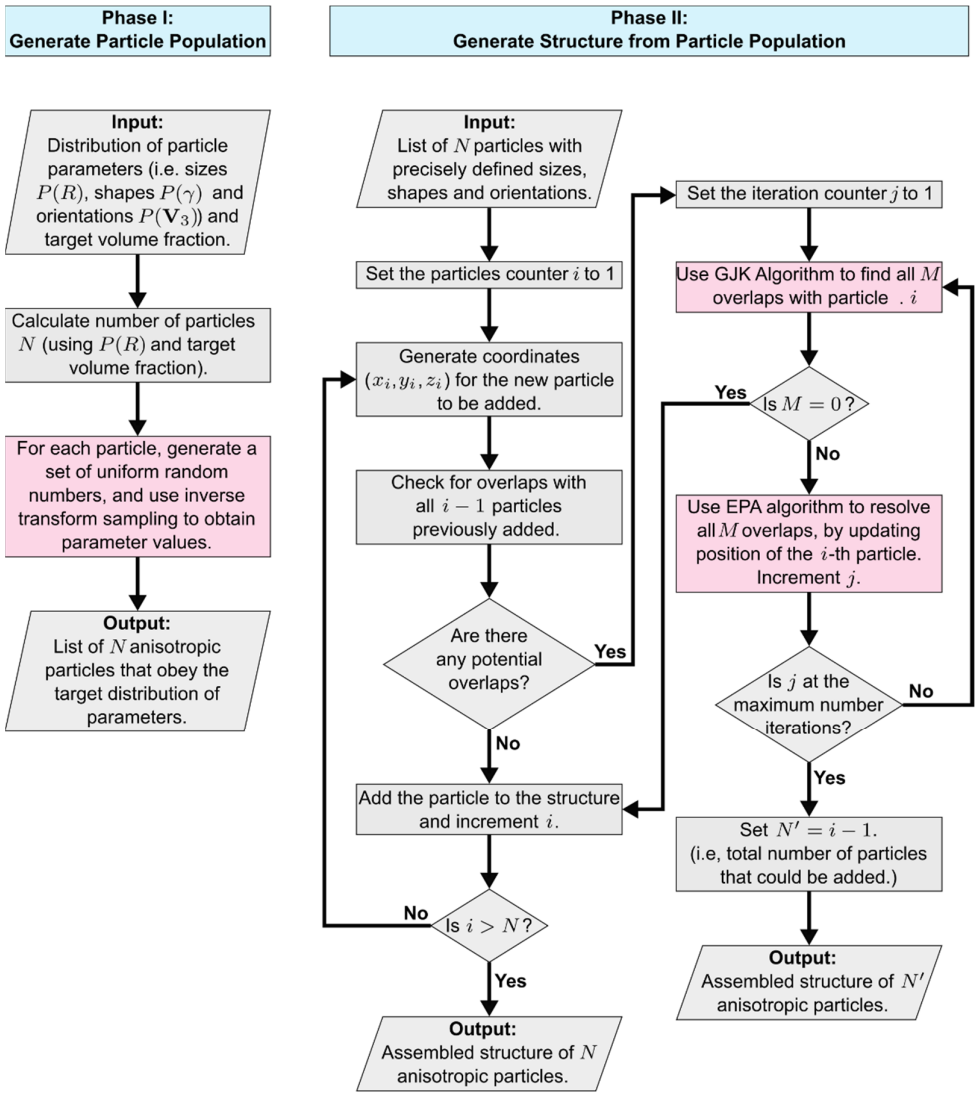

Figure 2 Flowchart of the steps involved in CASGAP subdivided into two phases. *Phase I* to generate population of particles for given input, and *Phase II* to assign coordinates to the particles and output the three-dimensional structure with desired positional and orientational order. The blocks shown with a reddish hue will be discussed in more detail in the text. GJK refers to the Gilbert-Johnson-Keerthi algorithm[43] and EPA refers to expanding polytope algorithm[44].

used software tools like *packmol*[47] and *LAMMPS*[48] have tackled similar challenges of anisotropic structure generation using discrete particle approximation where they use rigid groups of spherical particles as a single entity (sometimes treated as molecules). However, to the best of our knowledge, these tools currently have not directly tackled structure generation of non-spherical particles, and do not support imposition of statistical distributions to particle orientations.

Results and Discussion

Computational Approach for Structure Generation of Anisotropic Particles (CASGAP)

The steps of our new computational approach CASGAP are presented in the flowchart in **Figure 2**. The approach has been divided into two phases - *Phase I* builds a list of particles that follow a target distribution of parameters and *Phase II* builds the representative structure of particles by adding them sequentially without any overlaps. This division into two phases has been explained in more detail later and is preserved in the organization of the CASGAP source code. Our primary intention is to demonstrate that these phases are independent of each other, and the users can accordingly decide the best way to use this method for their purposes to perhaps only generate particle populations using *Phase I* or to use their own generated particle populations as input for *Phase II*.

In Phase I, the user provides input of the statistical information (e.g., mean, variance) or the probability distributions of the parameters related to particle shape, size, and orientational order. The attributes of these parameters are described in a later section. In general, assuming that one of the parameters is represented as X, such that for particle with index i, the

parameter value is X_i, the probability distribution of this parameter is defined by the density function $P(X)$ and the cumulative distribution function is $F_X(x) = P(X \leq x)$. The random sample X_i is then obtained by inverse transform sampling, where a uniform random number u_i, with $0 < u_i \leq 1$, is fed to the inverse of the cumulative distribution function: $F_X^{-1}(u_i) \equiv X_i$. The number of particles N in the list is estimated by evaluating the running total of all the particle volumes, calculating the volume fraction, and comparing it to a target volume fraction.

In Phase II, the list of particles from Phase I with precisely defined distributions of shape, size and orientation are sequentially placed within the 3D structure. Each of the coordinates x_i, , y_i or z_i of each new particle i, are first sampled from a uniform distribution over the interval $(-L/2, L/2]$ where L is the simulation box length. Before adding the particle to these coordinates, the method checks for overlap with all $i-1$ previously added particles in the structure. This step is expedited by using a bounding sphere, and checking whether the bounding spheres overlap. Only if they do, the particles are considered as potentially overlapping. The Gilbert-Johnson-Keerthi (GJK) algorithm[49] is then used to determine overlaps to a higher precision, and the expanding polytope algorithm (EPA)[50] is then used to resolve the overlap by updating x_i, y_i and z_i. Although this method attempts to incorporate all the particles in the list into the structure, the difficulty to add new particles increases as the density of particles increases. The method therefore attempts to add the particle by first locally shifting the particle, and intermittently trying new random locations, until either the particle finds an overlap-free position, or a maximum number of iterations are reached. If not all N particles could be added, the structure with $N' = i - 1$ particles is generated as output; the way the particles are placed ensures that even if the algorithm is terminated before all N particles are added the structure still adheres to the target statistical distributions of the particle shapes, sizes, and orientation parameters.

Before we describe all the relevant details of this method, we highlight a few strengths and capabilities of this method. The division of the method into two Phases allows for customization in these phases independently and makes the method more generalizable and easier to extend. Phase I can be highly specific to the modeling requirements with input parameters that can be simplified to enable model studies or made to achieve a more experimentally relevant representation. As an example of the latter, in experiments, synthesis procedures could give rise to high dispersity in particle shape and size and yet when assembled these non-uniform particles may exhibit domain sizes and shapes with low dispersity[51]. Another capability of the method is that it can be easily extended to include complexity in particle geometry where more parameters that influence particle geometry or order can be identified as the need arises. Phase II does not need to make any assumptions about the particle geometry and can take as input any population of particles generated by Phase I and create a structure with the desired input distribution of order parameters. In this regard, we highlight the use of GJK (and EPA) algorithms, originally used in aerospace engineering and video games, for our purpose to avoid inter-particle overlap and generate desired 3D structures of amorphous soft materials. These algorithms have had limited use in soft materials; to the best of our knowledge they have only been used in evaluation of pair potentials for anisotropic particles[52], Monte-Carlo method based pressure control for anisotropic particle self-assembly into superlattices[53], and discrete element modeling of granular particles[54].

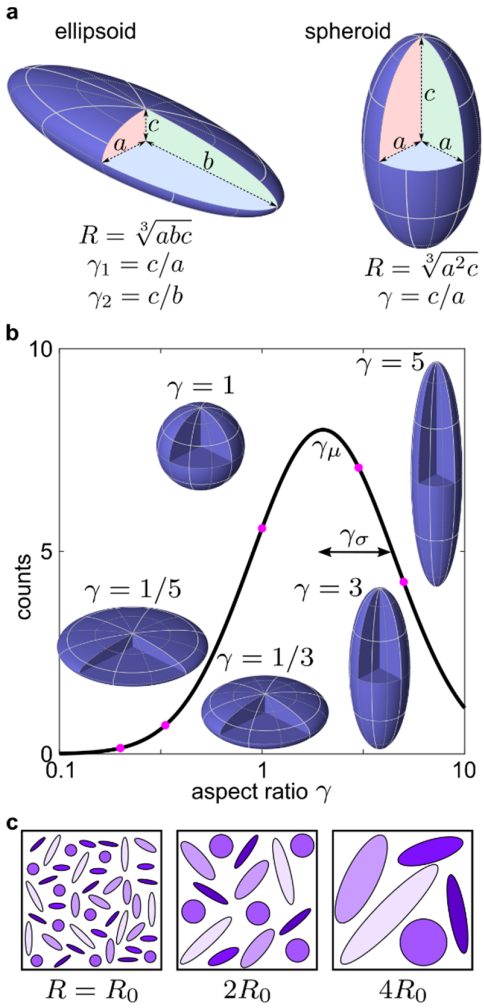

Figure 3 Distributions of particle shape and size. (a) Geometrical parameters of ellipsoids and spheroids. (b) Log-normal distribution of the aspect ratio γ (particle shape), with mean γ_μ and standard deviation γ_σ. Insets are used to show the shape variation of these with aspect ratio. (c) 2D cross-section profiles of spheroids at different R values as indicated. Within each square depicted in the insets, the shapes have the same R value and distinct colors are used to differentiate the shape with the darker shades being more oblate, and lighter shades being more prolate.

Details of Phase I: Generation of Particle Population

Distributions of particle geometry (shape and size): As our model anisotropic particles (**Figure 3a)** we select ellipsoids which are effectively perturbations of a sphere along the three

mutually perpendicular axial directions, with semi-axial lengths: a, b and c that simultaneously control the size and the aspect ratios of the ellipsoid. To define parameters that can decouple size and shape characteristics, we define the volumetric radius $R = \sqrt[3]{abc}$ and two aspect ratios $\gamma_1 = c/a$ and $\gamma_2 = c/b$ as parameters. The parameter R effectively depicts the size (or the volume) of the particles and parameters γ_1 and γ_2 the shape anisotropy of the particles for a given volume. In some cases, it can be realistic or advantageous to simplify this model further by only considering a cylindrically symmetric ellipsoid, also known as a *spheroid*, where $a = b$. In such cases, the particles can be modelled using R and γ (dropping the subscripts since $\gamma_1 = \gamma_2 \equiv \gamma$). The advantage for such simplification may become evident when experimental measurement of both aspect ratios is not possible or reliable, and an average aspect ratio is the best physical approximation. Moreover, as will be made clear later, the orientation of spheroids is easier to quantify and measure than an arbitrary ellipsoid.

In **Figure 3b**, we demonstrate how the shape of the spheroidal particles can vary from oblate ($\gamma < 1$) to prolate ($\gamma > 1$), and how dispersity in particle shapes can be modeled using a log-normal distribution. Log-normal distribution is an appropriate choice because it is strictly defined over the positive parameter values and is associated with the normal distribution. Note, however, that this is only a convenient choice, and to replicate the realistic population of particles synthesized more complicated distribution which may be multi-modal can be used; only restriction we impose is that the distribution should be defined over positive parameter values. The mean and the standard deviation of the 'particle shape' distribution, given by γ_μ and γ_σ become the structural parameters that need to be provided as inputs in Phase I. In an analogous manner, the dispersity in size R of the particles (**Figure 3c)** can be modeled using the log-normal distribution or any experimentally guided (more appropriate) distribution. The details of the log-normal distribution used and how they can be inverted to generate parameter values, are provided in the **Supplementary Materials Section S1**.

Distribution of orientational order among the spheroidal particles: The next set of structural parameters to consider are the orientational order of the particles. Particles with shape anisotropy like spheroids and ellipsoids, have a well-defined orientation which can be quantified by an n-dimensional unit vector $\boldsymbol{V}_n$, where n depends on the symmetry of the particle shape (and the dimensionality of the space, i.e., 2D vs 3D). For example, n can be 1 when an anisotropic shape is confined to 2D, such that only an angle with respect to a reference direction is required to quantify its orientation. For a spheroidal particle, the orientation can be expressed by tracking how its axis of rotational symmetry (the c-axis) can exist in 3D. We can use a 3D unit vector $\boldsymbol{V}_3 \equiv (\cos\theta \sin\phi, \sin\theta \sin\phi, \cos\phi) \equiv (\theta, \phi)$, which is expressed by two angles: θ (azimuthal component) and ϕ (polar component), as is common in the spherical coordinate system and where $0 \leq \theta < 2\pi$ and $0 \leq \phi \leq \pi$.

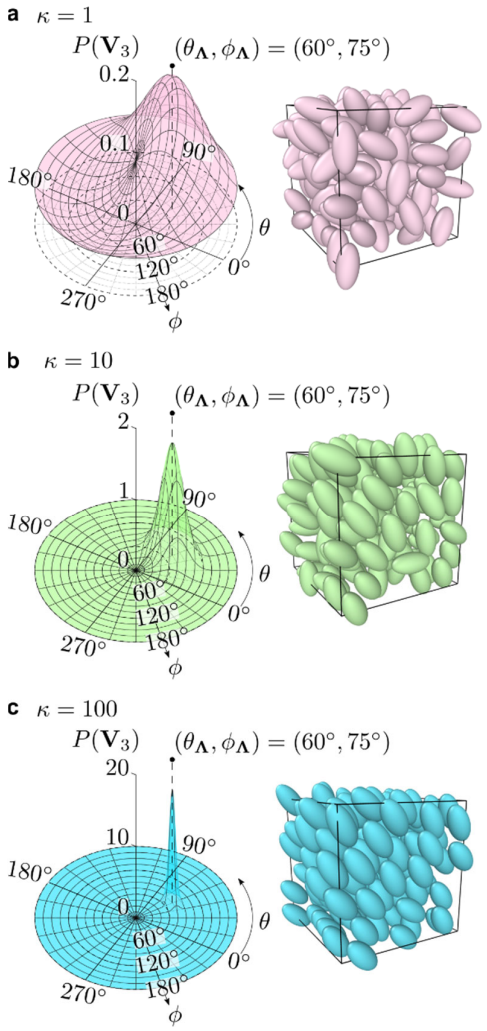

Figure 4 Distribution of orientational order among the spheroidal particles. The orientation of spheroids is represented by a 3D unit vector $\boldsymbol{V}_3$. (a-c) The von Mises-Fisher (vMF) distribution $P(\boldsymbol{V}_3)$ for $\boldsymbol{V}_3$ at $\kappa = 1$, 10 and 100 plotted as a polar plot where θ and ϕ angles corresponding to the spherical polar coordinates. The mean orientation is $\boldsymbol{\Lambda}_3$ whose spherical polar coordinates are $(1, \theta_\Lambda, \phi_\Lambda)$ where $\theta_\Lambda = 60°$ and $\phi_\Lambda = 75°$ as an example. On the right, the resulting spheroidal particle structures obeying the vMF distribution for the corresponding κ value is depicted.

In the above framework, we can also define a reference orientation $\boldsymbol{\Lambda}_3 \equiv (\theta_\Lambda, \phi_\Lambda)$ (also a unit vector) and check to see whether the particles are co-oriented with $\boldsymbol{\Lambda}_3$. To make a comparison between two orientations, we can use the magnitude of their dot product $p = |\boldsymbol{V}_3 \cdot \boldsymbol{\Lambda}_3|$ to quantify how well they match. Accordingly, p shall approach 1 if the orientations match perfectly and will be 0 if they are orthogonal (perpendicular). If the spatial arrangement of the anisotropic particles is isotropic, the orientations of all the constituent particles must be random. This can be demonstrated when the orientations of all the particles are compared to the same reference $\boldsymbol{\Lambda}_3$, such that p values will be evenly distributed over the 0 to 1 range, showing no preference to any particular value. On the other hand, if the distribution of p has a noticeable peak at any value over the 0 to 1 range, then the particles are co-

oriented, and the spatial arrangement of the anisotropic particles also has orientational anisotropy. In this situation, we can redefine $\boldsymbol{\Lambda}_3$ to also indicate the direction of preferred orientation as well as to serve as a reference. In directional statistics[55], one such distribution that can describe orientational anisotropy is the von Mises-Fisher (vMF) distribution as shown in **Figure 4**.

The vMF distribution is an appropriate choice for describing the orientational order in the particles' spatial arrangement because it is an analogue of the normal distribution defined on the surface of a sphere. Its probability density function is defined as $P(\boldsymbol{V}_3) = C(\kappa)\exp(\kappa\,\boldsymbol{\Lambda}_3 \cdot \boldsymbol{V}_3)$, where $\boldsymbol{\Lambda}_3$ will serve as the mean (or preferred) orientation, κ is technically referred to as the concentration parameter, and $C(\kappa)$ is a normalization constant. We shall, however, avoid the usage of the term "concentration parameter" as it may cause some unintentional confusion with the use of the term "concentration" in Chemistry and instead, in this paper we shall refer to κ as the orientational-anisotropy parameter. This is because κ directly quantifies the extent of orientational order, with $\kappa = 0$ for lack of orientational order and $\kappa \to \infty$ for high orientation anisotropy. As shown in **Figure 4,** for nonzero κ, the vMF distribution produces a peak near the $\boldsymbol{\Lambda}_3$ value, and the dispersity proportional to the reciprocal of κ.

So far, we have described orientation order only for spheroids, but more generally, if the ellipsoidal particles have lower symmetry, such that $\gamma_1 \neq \gamma_2$, we can more generally employ a four-dimensional unit vector $\boldsymbol{V}_4$, also known as unit-quaternions, to characterize their orientation. This is because for two non-spheroidal ellipsoids to have the same orientation, all their corresponding axes should align together, and simply aligning one of their axes (as was the case in spheroids) is not sufficient. In simple terms, a unit-quaternion can be expressed by a combination of a scalar angle ω and a 3D unit vector $\boldsymbol{w} = (w_1, w_2, w_3)$, so that we can define $\boldsymbol{V_4}$ as:

$$\boldsymbol{V_4} \equiv (\omega, \boldsymbol{w}) = (\cos(\omega/2), \sin(\omega/2)\,w_1, \sin(\omega/2)\,w_2, \sin(\omega/2)\,w_3) \quad (1).$$

In **Figure 5a** (on the left), an ellipsoid with axes aligned to the coordinate axes is defined to have a zero orientation with $\boldsymbol{V}_4 \equiv 0$. If this ellipsoid is then rotated by the angle ω about the vector $\boldsymbol{w}$ passing through the origin following the right-hand rule (as shown on the right), then the orientation of the ellipsoid is given by equation (1). Note that for zero orientation, $\boldsymbol{V}_4 = 0$ can be equivalently written as $\boldsymbol{V}_4 = (0, \boldsymbol{w})$ indicating that the angle of rotation is zero ($\omega = 0$), and we do not need to explicitly mention a $\boldsymbol{w}$ vector as it can be any arbitrary vector about which a rotation is not performed. Variation of orientation for a non-spheroidal ellipsoid $\boldsymbol{V}_4$ can also be modeled using the vMF distribution with $P(\boldsymbol{V}_4) = C(\kappa)\exp(\kappa\,\boldsymbol{\Lambda}_4 \cdot \boldsymbol{V}_4)$, where $\boldsymbol{\Lambda}_4$ is the mean orientation and κ is the orientational-anisotropy parameter (same as for spheroidal orientation).

As can be expected, $P(\boldsymbol{V}_4)$ is difficult to visualize without using more than three-dimensions, however it behaves in an

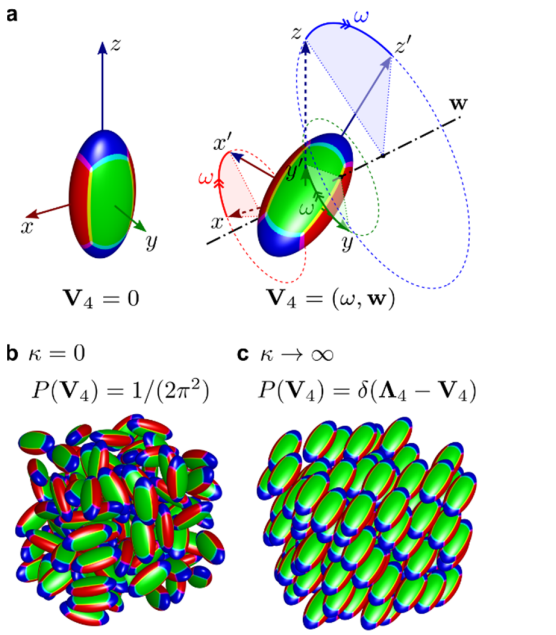

Figure 5 Distribution in orientation for ellipsoidal particles with dissimilar aspect ratios. (a) (Left) An ellipsoid with axes aligned perfectly to the reference axes x, y, z. (Right) The ellipsoid after being rotated along w by an angle ω such that its axes change from $x, y, z \to x', y', z'$. The dashed circles show the trajectory of the rotating axis. (b, c) Ellipsoidal particle structures following the vMF distribution $P(\boldsymbol{V_4})$ for $\boldsymbol{V_4}$ (which cannot be plotted) for $\kappa = 0$ (highly isotropic) and approaching ∞ (highly anisotropic). The vMF distribution for (b) is a uniform distribution with $P(\boldsymbol{V_4}) = 1/2\pi^2$ (a constant), and for (c) is a Dirac-delta function about Λ_4 with $P(\boldsymbol{V_4}) = \delta(\boldsymbol{\Lambda_4} - \boldsymbol{V_4})$. All ellipsoids are identical and colored with red, green, blue regions to allow easy visualization of their orientations.

analogous manner as $P(\boldsymbol{V}_3)$ in **Figure 4**, with κ having an analogous behavior. In **Figures 5b** and **5c,** we demonstrate the spatial arrangement obtained for the extreme values of κ parameter. When $\kappa = 0$, the vMF distribution reduces to the uniform distribution on the surface of a 4D hypersphere, meaning that each orientation is equally likely to occur (i.e., isotropic arrangement orientationally) and $P(\boldsymbol{V}_4) = 1/(2\pi^2)$, which is a uniform distribution, and the constant is obtained by normalizing with the surface area of a unit hypersphere which is $2\pi^2$. On the other hand, when $\kappa \to \infty$ in **Figure 5c**, the peak of the vMF distribution sharpens to the extent that $P(\boldsymbol{V}_4) \to \delta(\boldsymbol{\Lambda}_4 - \boldsymbol{V}_4)$, where $\delta(\cdot)$ is the Dirac-delta function, and all ellipsoids have the same orientation.

One key point not to be missed is that even for non-spheroidal ellipsoids, one may choose to represent their orientation with $\boldsymbol{V}_3$ (a 3D vector) by for example, keeping track of only one axial direction (like the c-axis). This can be done to intentionally be agnostic about the other axial directions which may rotate freely as per modeling requirements. The 4D vector orientation $\boldsymbol{V}_4$ has been included to have more general representation of orientation for non-spheroidal ellipsoids, which may be important when trying to optimize the structure to better fit an experimental scattering profile (e.g., as a possible future extension of the CREASE[32] method). In any case, the mean orientation $\boldsymbol{\Lambda}_3$ (or $\boldsymbol{\Lambda}_4$) and κ are the structural parameters that

can be provided as input in Phase I. Generating random samples of particle orientation requires, requires some additional steps which are described in the **Supplementary Materials Section S2**, and more comprehensively covered in refs.[56–58]

Details of Phase II: Generation of Structure from Particle Population

At the end of Phase I we have a list of particles that have desired distributions of shapes and sizes. In Phase II we place these particles one-by-one into a representative 3D spatial arrangement. As noted earlier, a particle is successfully placed if it avoids any overlap with other previously added particles. Detection of overlap is simplified by eliminating all particles that completely lie outside the bounding sphere of the i-th particle. For two anisotropic particles, if the sum of their bounding sphere radii is smaller than their center-to-center distance, then those particles can never overlap. On the other hand, if the sum of the bounding sphere radii is greater, then a more sophisticated method (than that for spheres) is needed to evaluate whether they overlap. In the example of ellipsoidal particles, ellipsoid-ellipsoid intersection itself has been a topic of great interest in many areas of scientific research[59,60], including those relevant to soft materials for example in calculating the excluded volume effects of particles[61,62]. Notably, the work by Zheng et al.[63] describes a strategy to compute the distance of closest approach between two ellipsoids by first finding the distance of closest approach between two elliptical cross-sections analytically, and then rotating the plane by numerical computation to minimize that distance.

It is however our intention not to be restricted to ellipsoidal particles, and Phase II is more general to an anisotropic particle with any arbitrary geometry or shape. In fact, in Phase II, if the output of Phase I is used with ellipsoidal particle geometry, a preliminary step is to convert the ellipsoidal shapes to convex polyhedral shapes (that completely bounds the ellipsoids), to make computations regarding overlaps simpler. Subsequently, as mentioned before, collision detection algorithms from the aerospace engineering field are used to find and resolve overlaps between these bounding convex polyhedral shapes. An advantage of using convex polyhedral shapes is the property that such shapes can be uniquely defined by the position of their vertices. However, care must be taken to minimize the volume difference between the ellipsoidal particle and the bounding polyhedron, so that their overlap avoidance does not waste extra space by positioning the actual particles further away from each other than necessary.

These steps for Phase II are schematically depicted in **Figure 6a**, where two overlapping ellipsoidal particles are first converted to corresponding convex polyhedral shapes. The GJK algorithm[49,50] is then adapted to work on the polyhedral shapes to detect whether they overlap. If the two shapes overlap, then an extension of the GJK algorithm called EPA is used to find the

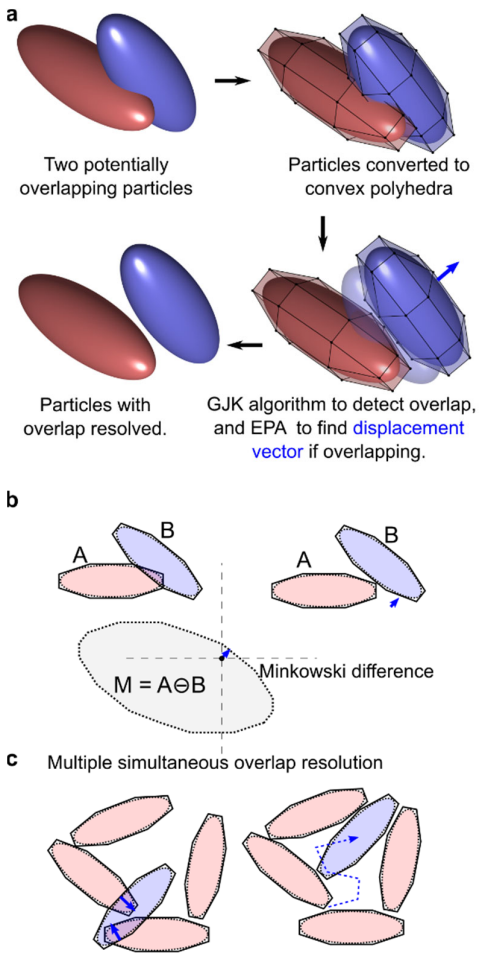

Figure 6 Overlap Detection and Resolution. (a) Schematic representation of overlap resolution of two ellipsoidal particles, which are first converted to their convex polyhedra, and then GJK and EPA algorithms, respectively, detect the overlap, and determine the displacement vector. (b) The situation in (a) represented in 2D to show the Minkowski difference of their shape which is at the heart of the GJK and EPA algorithms. (c) Resolution of multiple overlaps by addition of pair-wise displacements for the new particle, and iteratively moving the new particle until no further overlaps are detected.

minimum displacement vector which will resolve the overlap if one of the particles is moved along that vector.

Although the complete details of how the GJK and EPA algorithms work is beyond the scope of this work, we describe some of the relevant details here and direct the reader for additional information in the **Supplementary Material Sections S3 and S4.**

The main idea behind the GJK and EPA algorithms is schematically shown in **Figure 6b** with 2D representation of the particles and their bounding polygonal shapes (A and B), which involves the construction of a composite shape M called the Minkowski difference, denoted as $\mathrm{M} = \mathrm{A} \ominus \mathrm{B}$, obtained by subtracting all the points in shape B from shape A, as explained in supplementary material section S3 . Knowing shape M enables us to reformulate the problem of finding overlap between two convex polyhedral shapes, into a problem of

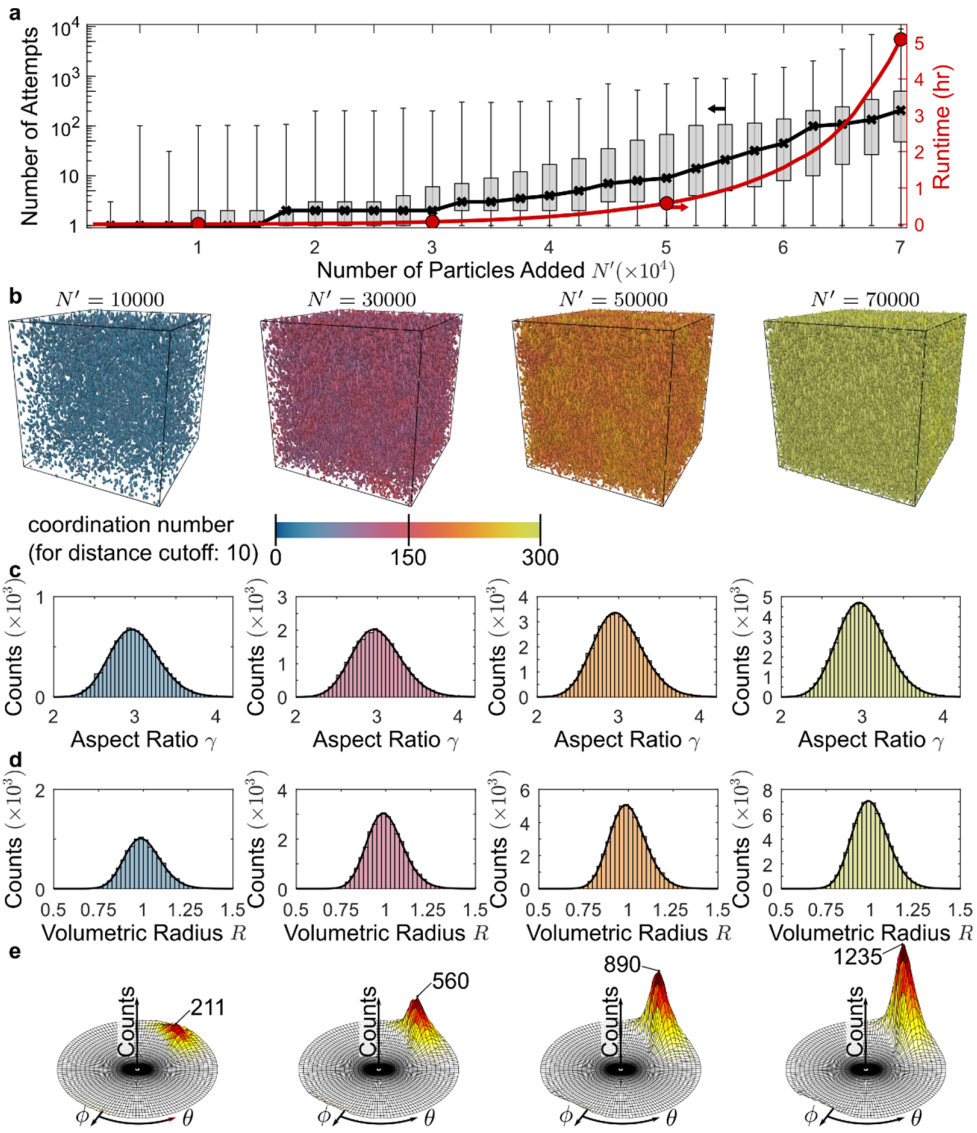

Figure 7 Statistical properties of generated structure at different particle populations. In this example, the length of the simulation cell is 100 units, γ and R are both log-normally distributed with means 3 and 1 units, respectively, and standard deviations for both is fixed to 10% of the mean value. The orientation is distributed using the vMF distribution with mean orientation $\boldsymbol{\Lambda_3} = (-120°, 75°)$ and $\kappa = 10$. (a) (left axis) Box plot showing the number of attempts per 2500 particles added, the interquartile range as well as the minimum and maximum attempts in that interval. The solid curve connects the median number of attempts marked by cross symbols. The right axis shows the runtime of the method as particles are assembled into the structure. Runtime (hr) of the method is based on performance on a single Intel Xeon E5v4 processor running at 2.10 GHz (single-threaded). Filled circles mark the particle populations N' at which the generated structure is checked for adherence to target statistics. (b) Generated structures at different N' with particles colored by their coordination number, calculated using a cutoff radius of 10 units. (c,d) Histograms showing the adherence to the log-normally distributed aspect ratio and volumetric radius, respectively of the structures with different N' shown in (b). The target distributions in each case are overlayed as solid black curves and normalized to N'. (e) Surface plot of histogram showing the adherence to vMF distribution for particle orientation (target distribution is not shown for clarity). The count of particles at the peak (which is the mean orientation) is noted for each case.

finding whether the origin lies inside shape M, which is easier to solve. If the origin lies inside M then the shapes overlap, otherwise they do not. Moreover, if shape M contains the origin, the shortest vector that connects its surface to the origin is the displacement vector that will resolve the particle overlap as shown in **Figure 6b**. As described in more detail in the supplementary material section S4, the GJK and EPA algorithms work on the reformulated problem of determining whether origin is inside M and if so, what is the displacement vector that will resolve the overlap, respectively.

During Phase II, it is easy to imagine the situation, especially at high particle density, that a new particle i (that needs to be added), overlaps with several particles simultaneously as shown in **Figure 6c**. In this case, EPA provides displacement vectors in a pair-wise manner, and our method adds these displacements together to determine a cumulative displacement vector, that we use to move particle i. In this process, sometimes the individual pair-wise displacements may cancel, and particle i still intersects with other particles. Therefore, an iterative scheme is employed until a maximum number of iterations is

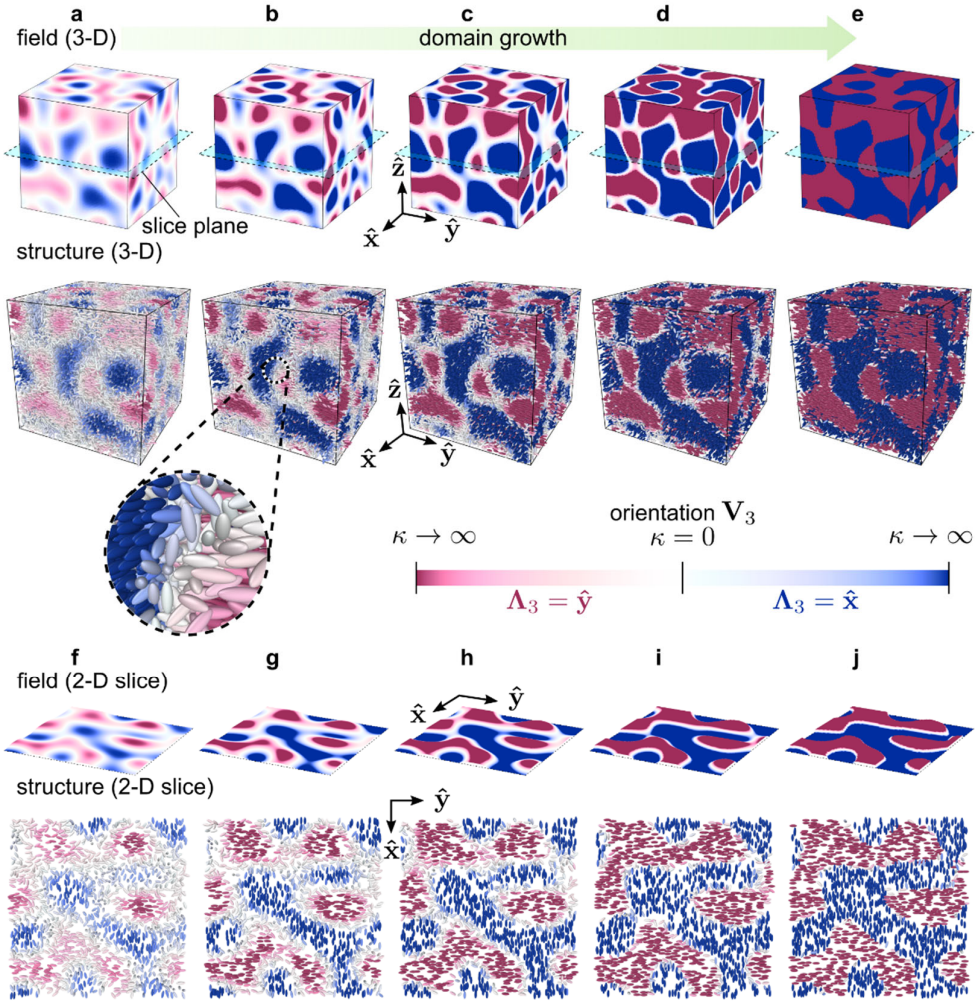

Figure 8 Application of method to study growth of aligned domains. (a-e) Orientational field and generated structure of particles in 3D showing an evolution in the size of the domains. The inset shows a zoomed-in view of the structure to reveal the particle shapes. (f-j) Corresponding cross-sectional view of the orientational field and structure showing the degree of alignment as the field evolves. The cross-sectional plane in (f-j) is labeled "slice plane" in (a-e, marked by dashed lines). In each instance, the field evolution is achieved by controlling the f_{cut} values as (a,f) 1, (b,g) 0.75, (c,h) 0.5, (d,i) 0.25 and (e,j) 0.

reached, to find a position where particle i finds a location without any overlap. Intermittently, the method also regenerates completely new random coordinates x_i, y_i, z_i for particle i, to avoid getting stuck inside small empty holes, or particle gaps which can never fit particle i.

As Phase II proceeds and as the particle density increases, the availability of empty space decreases, and as a result multiple attempts are needed to find positions for newer particles. This is shown in **Figure 7**, where number of attempts are plotted (on the left axis) with respect to the population of particles N' in the form of box plots per 2,500 particles added. This shows how much variation can be expected within this interval of addition, showing initially that maximum number of attempts are within 100 attempts for about 20,000 particles added, but as more particles are added, the maximum number of attempts can reach up to 10,000 attempts after which a position for that particle was found. In all the intervals, the minimum number of attempts has been 1, indicating that some particles are still able to find an empty spot at their first trial. However, as shown from the median curve (solid black), most particles need more attempts as the population increases. This also means that the runtime of the method increases, and the growth of the time seems to be exponential. For this reason, it may be advantageous to stop the method earlier and use the generated structure with fewer particles than initially intended, for further analysis as required.

Our method ensures that even upon early termination, the 3D structure of particles follows the target distributions of particle shape, size, and orientational order. **Figures 7b** and **7c** demonstrate that when the generated structure is examined at various stages, with values of N' ranging from 10,000 to 70,000 all the distributions closely match the targeted log-normal distributions for shape and size. Furthermore, in **Figure 7d**, snapshots of the structure are shown with particles colored by their coordination number, which measures the number of

neighboring particles within a cutoff radius of 10 units. The homogeneity in the coloring indicates that particles are added uniformly throughout the volume. The homogeneity of particle addition is further demonstrated in **Supplementary Video S1**. Finally, in **Figure 7e**, for each of the corresponding structures in **Figure 7d**, the histograms of orientation of the particles show the adherence to the vMF distribution.

Example Modification to the Method to Model Growth of Aligned Domains

The applications that originally motivated the development of CASGAP is the use of the generated 3D real space structure(s) with desired distributions of particle shape, size and orientational order as initial configuration for follow-up calculations (e.g., computing the structure's scattering profile to enable use of machine-learning enhanced CREASE[32,64], conducting finite difference time domain method for color response prediction[65]). Another potential application is creating 3D structures to understand dynamics during 3D printing of soft/hybrid materials[66,67] with a specific external stimulus (e.g., light) or field (e.g., electric/magnetic) applied during printing that creates spatial correlation or fields within the structure. To model structures in these applications, it becomes important to include spatial (auto) correlations for a specific parameter, as it pertains to the specific scattering profile or property.

We demonstrate an extension of the CASGAP method to include spatial correlations for one specific parameter during creation of the 3D structure. In the example shown in **Figure 8**, we apply the modified CASGAP method to create a structure with particles oriented according to spatial random field of particle orientation. A spatial random field $g(x,y,z)$ can be chosen to obey the standard normal distribution (easily generated using several approaches[68]), i.e., the intensity range of $g(x,y,z)$ is $(-\infty,\infty)$, mean and standard deviation of $g(x,y,z)$ are 0 and 1, respectively. This field can be easily converted to have a uniform distribution by using the error function transformation, $f(x,y,z)=\mathrm{erf}\big(g(x,y,z)\big)$, such that the range of intensities of $f(x,y,z)$ are now bounded to $(-1,1)$ while preserving the same spatial correlations as $g(x,y,z)$. This field $f(x,y,z)$ is presumed to contain orientational correlation information of a two phase system of anisotropic particles, with the sign of $f(x,y,z)$ indicating the preferred orientation ($\boldsymbol{\Lambda}_3$ under the vMF distribution), and the magnitude of $f(x,y,z)$ indicating the dispersity in orientation (κ under the vMF distribution). This is shown in **Figure 8**, with the negative values (in blue) of the field are assigned to the phase with preferred orientation $\boldsymbol{\Lambda}_3=\hat{\boldsymbol{x}}$, and positive values (in maroon) are assigned to the phase with $\boldsymbol{\Lambda}_3=\hat{\boldsymbol{y}}$. Furthermore, using the description of the vMF distribution, we convert the field values into κ values by using $\kappa=(|f(x,y,z)|^{-1}-1)^{-1}$, which gives $\kappa=0$ when $f(x,y,z)=0$ and $\kappa\to\infty$ when $f(x,y,z)=\pm1$.

Using the field-based input for particle orientations, the CASGAP method needs the following modifications. (1) In *Phase I* particle shapes and sizes are generated according to the user specified distributions, however, particle orientations are not generated. (2) In *Phase II,* when particle i is being added, its newly generated coordinate (x_i,y_i,z_i) is used to evaluate the field value $f(x_i,y_i,z_i)$, and then as described above converted to the corresponding vMF distribution values ($\boldsymbol{\Lambda}_3$,κ). The particle orientation is then randomly sampled from the vMF distribution. (3) Once the orientation is designated, the particle is assessed for overlap using the same method described for Phase II. If the particle is displaced from its previous location due to overlap, then up to a small displacement the particle is allowed to remain, otherwise the field is reevaluated at the new location, and the subsequent process is repeated iteratively. This continues until either a valid configuration is achieved or if the method terminates.

Using this modification, we now demonstrate how this method can also generate structures where the underlying field evolves systematically. In **Figure 8**, we have evolved the field to $h(x,y,z)$, by using a positive field cutoff value f_{cut}, where $0\le f_{cut}\le 1$, such that

$$h(x,y,z)=\begin{cases}1, & f(x,y,z)>f_{cut}\\ \dfrac{f(x,y,z)}{f_{cut}}, & |f(x,y,z)|\le f_{cut}\\ -1, & f(x,y,z)<-f_{cut}\end{cases}. \qquad (2)$$

The effect of this evolution for values of f_{cut} ranging from 0 to 1 is shown in **Figure 8** (a-e for 3D, and f-j for 2D slice) and causes a growth of the domains. Accordingly, the structures generated from this field evolution follow the same trend with the darker shaded regions having particles that are increasingly co-oriented. In **Figure 8f-8j**, a slice plane of the field and the structures is also shown, which clearly demonstrates how the particles align with the $\hat{\boldsymbol{x}}$ or $\hat{\boldsymbol{y}}$ depending on the phase domain they occupy. In this example, we have elected to keep the particle size and shape similar, and only varied the orientation of the particles to remove any ambiguity in visualization of the results. In principle, we can also extend the above approach to create field-based description of particle sizes and shapes that mimic gradient effects during synthesis (causing a spatial effect on particle size and shape) and deposition of particles in a film.

Conclusions

In this study we have demonstrated the steps in our novel computational method - Computational Approach for Structure Generation of Anisotropic Particles (CASGAP) - that can generate a real space 3D structure of anisotropic particles with (1) all particle parameters such as shape, size and orientation distributed according to a target statistical model, or alternatively (2) with some particle parameters described by a spatial field description, while the rest of the parameters having a target statistical model. The method ensures that at each incremental stage of structure generation, the particles always adhere to the desired particle shapes, sizes and orientations

described by the input distributions, which enables early termination based on computational resource/time constraints to use the already generated structure for further analysis. The structures generated from this CASGAP method can be used to study interpret structural characterization of soft materials from small angle scattering experiments, simulating processing effects especially using the field-based structure generation, provide initial configurations for additional physics-based molecular simulations to evolve structures or numerical simulations to calculate physical properties (e.g., mechanical strength, color, optical response, etc.).

Methods

The CASGAP code has been implemented using MATLAB version R2022a (MathWorks, Natick, MA). The code is available via https://github.com/arthijayaraman-lab/casgap (link currently inactive). We are also making the code available in Python on the same repository.

Author Contributions

A.J. and N.G. conceptualized the idea. N.G. developed the methodology, performed all analysis and visualization with A.J. providing supervision. Both A.J. and N.G. were involved in the writing and editing of the manuscript.

Conflicts of interest

There are no conflicts to declare.

Acknowledgements

The authors acknowledge financial support from the Air Force Office of Scientific Research (MURI-FA 9550-18-1-0142). Computational resources were provided by the University of Delaware's Caviness cluster. Authors thank Mr. Sri Vishnuvardhan Reddy Akepati for his efforts and contributions in converting the CASGAP source code from MATLAB to Python.

Notes and references

1 I. W. Hamley, *Introduction to Soft Matter: Polymers, Colloids, Amphiphiles and Liquid Crystals*, John Wiley & Sons, Chichester, 2000.
2 Z. M. Sherman, M. P. Howard, B. A. Lindquist, R. B. Jadrich and T. M. Truskett, *J. Chem. Phys.*, 2020, **152**, 140902.
3 L.-T. Yan and X.-M. Xie, *Prog. Polym. Sci.*, 2013, **38**, 369–405.
4 F. L. Paiva, A. R. Secchi, V. Calado, J. Maia and S. Khani, *Macromolecules*, 2021, **54**, 4198–4210.
5 C. J. Stender, E. Rust, P. T. Martin, E. E. Neumann, R. J. Brown and T. J. Lujan, *Biomech. Model. Mechanobiol.*, 2018, **17**, 543–557.
6 S. Paszkiewicz, I. Irska, A. Zubkiewicz, A. Szymczyk, E. Piesowicz, Z. Rozwadowski and K. Goracy, *Polymers*, 2021, **13**, 397.
7 G. B. Messaoud, P. Le Griel, D. Hermida-Merino and N. Baccile, *Soft Matter*, 2020, **16**, 2540–2551.
8 V. Calabrese, S. Varchanis, S. J. Haward, J. Tsamopoulos and A. Q. Shen, *J. Colloid Interface Sci.*, 2021, **601**, 454–466.
9 H. Fudouzi, *Sci. Technol. Adv. Mater.*, 2011, **12**, 064704.
10 M. Qin, M. Sun, M. Hua and X. He, *Curr. Opin. Solid State Mater. Sci.*, 2019, **23**, 13–27.
11 W. Man, M. Florescu, E. P. Williamson, Y. He, S. R. Hashemizad, B. Y. Leung, D. R. Liner, S. Torquato, P. M. Chaikin and P. J. Steinhardt, *Proc. Natl. Acad. Sci. U.S.A.*, 2013, **110**, 15886–15891.
12 H. Yu, *Prog. Polym. Sci.*, 2014, **39**, 781–815.
13 S. Mula, L. Donà, B. Civalleri and M. A. Van Der Veen, *ACS Appl. Mater. Interfaces*, 2022, **14**, 50803–50814.
14 A. Zhukov, Ed., *High performance soft magnetic materials*, Springer, 2017, vol. 252.
15 J. Popovic, D. Brandell, S. Ohno, K. B. Hatzell, J. Zheng and Y.-Y. Hu, *J. Mater. Chem. A.*, 2021, **9**, 6050–6069.
16 M. J. Park and S. Y. Kim, *J. Polym. Sci. B Polym. Phys.*, 2013, **51**, 481–493.
17 P. Jiang, J. Bertone, K. S. Hwang and V. Colvin, *Chem. Mater.*, 1999, **11**, 2132–2140.
18 X. Ye, L. Jin, H. Caglayan, J. Chen, G. Xing, C. Zheng, V. Doan-Nguyen, Y. Kang, N. Engheta, C. R. Kagan, and others, *ACS Nano*, 2012, **6**, 2804–2817.
19 C. Fernández-Rico, M. Chiappini, T. Yanagishima, H. de Sousa, D. G. Aarts, M. Dijkstra and R. P. Dullens, *Science*, 2020, **369**, 950–955.
20 B. Sun and H. Sirringhaus, *Journal of the American Chemical Society*, 2006, **128**, 16231–16237.
21 Y. Nagaoka, H. Zhu, D. Eggert and O. Chen, *Science*, 2018, **362**, 1396–1400.
22 I. Buttinoni, M. Steinacher, H. T. Spanke, J. Pokki, S. Bahmann, B. Nelson, G. Foffi and L. Isa, *Phys. Rev. E*, 2017, **95**, 012610.
23 K. M. Bratlie, H. Lee, K. Komvopoulos, P. Yang and G. A. Somorjai, *Nano Lett.*, 2007, **7**, 3097–3101.
24 F. Lin, X. Lu, Z. Wang, Q. Lu, G. Lin, B. Huang and B. Lu, *Cellulose*, 2019, **26**, 1825–1839.
25 F. A. Shah, E. Zanghellini, A. Matic, P. Thomsen and A. Palmquist, *Calcif. Tissue Int.*, 2016, **98**, 193–205.

26 K. J. Busam, C. Charles, G. Lee and A. C. Halpern, *Mod. Pathol.*, 2001, **14**, 862–868.
27 D. Lombardo, P. Calandra and M. A. Kiselev, *Molecules*, 2020, **25**, 5624.
28 N. N. Boustany, S. A. Boppart and V. Backman, *Annu. Rev. Biomed. Eng.*, 2010, **12**, 285–314.
29 P. A. Penttilä, L. Rautkari, M. Österberg and R. Schweins, *J. Appl. Crystallogr.*, 2019, **52**, 369–377.
30 R. McGreevy and L. Pusztai, *Mol. Simul.*, 1988, **1**, 359–367.
31 G. Tóth, *J. Mol. Liq.*, 2006, **129**, 108–114.
32 C. M. Heil, A. Patil, A. Dhinojwala and A. Jayaraman, *ACS Cent. Sci.*, 2022, **8**, 996–1007.
33 C. M. Heil, A. Patil, B. Vanthournout, S. Singla, M. Bleuel, J.-J. Song, Z. Hu, N. C. Gianneschi, M. D. Shawkey, S. K. Sinha, Jayaraman, Arthi, and Dhinojwala, Ali, *Sci. Adv.*, 2023, **9**, eadf2859.
34 Z. Wu and A. Jayaraman, *Macromolecules*, 2022, **55**, 11076–11091.
35 M. G. Wessels and A. Jayaraman, *ACS Polymers Au*, 2021, **1**, 153–164.
36 E. Lozano, D. Roehl, W. Celes and M. Gattass, *Comput. Math. with Appl.*, 2016, **71**, 1586–1601.
37 W. Jodrey and E. Tory, *Phys. Rev. A*, 1985, **32**, 2347.
38 W. Jodrey and E. Tory, *Powder Technol.*, 1981, **30**, 111–118.
39 S. Torquato and Y. Jiao, *Phys. Rev. E*, 2010, **82**, 061302.
40 S. Torquato and Y. Jiao, *Nature*, 2009, **460**, 876–879.
41 X. Jia and R. A. Williams, *Powder technology*, 2001, **120**, 175–186.
42 C. F. Schreck, N. Xu and C. S. O'Hern, *Soft Matter*, 2010, **6**, 2960–2969.
43 T. Börzsönyi and R. Stannarius, *Soft Matter*, 2013, **9**, 7401–7418.
44 H. Altendorf and D. Jeulin, *Phys. Rev. E*, 2011, **83**, 041804.
45 S. Xu, Y. Jin and Y. J. Lee, *Journal of the American Chemical Society*.
46 P. Kubala, P. Batys, J. Barbasz, P. Weroński and M. Cieśla, *Adv. Colloid Interface Sci.*, 2022, **306**, 102692.
47 L. Martínez, R. Andrade, E. G. Birgin and J. M. Martínez, *J. Comput. Chem.*, 2009, **30**, 2157–2164.
48 A. P. Thompson, H. M. Aktulga, R. Berger, D. S. Bolintineanu, W. M. Brown, P. S. Crozier, P. J. in't Veld, A. Kohlmeyer, S. G. Moore, T. D. Nguyen, Shan, Ray, Stevens, Mark J, Tranchida, Julien, Trott, Christian, and Plimpton, Steven J, *Comput. Phys. Commun.*, 2022, **271**, 108171.
49 E. G. Gilbert, D. W. Johnson and S. S. Keerthi, *IEEE J. Robotics Automat.*, 1988, **4**, 193–203.
50 G. Van Den Bergen, *Collision detection in interactive 3D environments*, CRC Press, Boca Raton, 2004.
51 V. Sharma, K. Park and M. Srinivasarao, *Mater. Sci. Eng. R Rep.*, 2009, **65**, 1–38.
52 V. Ramasubramani, T. Vo, J. A. Anderson and S. C. Glotzer, *J. Chem. Phys.*, 2020, **153**, 084106.
53 J. A. Millan, D. Ortiz, G. Van Anders and S. C. Glotzer, *ACS Nano*, 2014, **8**, 2918–2928.
54 S. Zhao and J. Zhao, *Comput. Phys. Commun.*, 2021, **259**, 107670.
55 K. V. Mardia, P. E. Jupp and K. Mardia, *Directional Statistics*, J. Wiley, New York, 2000, vol. 2.
56 G. Kurz and U. D. Hanebeck, in *2015 Sensor Data Fusion: Trends, Solutions, Applications (SDF)*, IEEE, 2015, pp. 1–6.
57 G. Ulrich, *J. R. Stat. Soc., C: Appl. Stat.*, 1984, **33**, 158–163.
58 A. T. Wood, *Commun. Stat. Simul.*, 1994, **23**, 157–164.
59 H. Ouadfel and L. Rothenburg, *Comput. Geotech.*, 1999, **24**, 245–263.
60 A. Nemirovski, C. Roos and T. Terlaky, *Math. Program.*, 1999, **86**, 463–473.
61 J. Rallison and S. Harding, *J. Colloid Interface Sci.*, 1985, **103**, 284–289.
62 J. Talbot, D. Kivelson, M. Allen, G. Evans and D. Frenkel, *J. Chem. Phys.*, 1990, **92**, 3048–3057.
63 X. Zheng, W. Iglesias and P. Palffy-Muhoray, *Phys. Rev. E*, 2009, **79**, 057702.
64 C. M. Heil, Y. Ma, B. Bharti and A. Jayaraman, *JACS Au*, 2023, **3**, 889–904.
65 A. Patil, C. M. Heil, B. Vanthournout, M. Bleuel, S. Singla, Z. Hu, N. C. Gianneschi, M. D. Shawkey, S. K. Sinha, A. Jayaraman, and others, *Adv. Opt. Mater.*, 2022, **10**, 2102162.
66 Q. Ge, B. Jian and H. Li, *Forces Mech.*, 2022, 100074.
67 L.-Y. Zhou, J. Fu and Y. He, *Adv. Funct. Mater.*, 2020, **30**, 2000187.
68 Y. Liu, J. Li, S. Sun and B. Yu, *Comput. Geosci.*, 2019, **23**, 1011–1047.